






Exploring the crystallization path of lithium disilicate through metadynamics simulations

Federica Lodesani ¹, Francesco Tavanti ^{1,2}, Maria Cristina Menziani ¹, Kei Maeda,³ Yoichi Takato,⁴ Shingo Urata ⁵ and Alfonso Pedone ^{1,*}

¹Department of Chemical and Geological Sciences, University of Modena and Reggio Emilia, via G. Campi 103, 41125 Modena, Italy

²CNR-NANO Research Center S3, Via Campi 213/a, 41125 Modena, Italy

³Department of Materials Science and Technology, Tokyo University of Science, Tokyo 125-8585, Japan

⁴Innovative Technology Laboratories, AGC Inc., Yokohama, Kanagawa 230-0045, Japan

⁵Planning Division, AGC Inc., Yokohama, Kanagawa 230-0045, Japan



(Received 23 January 2021; accepted 16 July 2021; published 30 July 2021)

Understanding the crystallization mechanism in silica-based materials is of paramount importance to comprehend geological phenomena and to design novel materials for a variety of technological and industrial applications. In this work, we show that metadynamics simulations can effectively overcome a large energy barrier to crystallize from viscous oxide glass melts and can be used to identify the melt-to-crystal transition path of the lithium disilicate system. The accelerated atomistic simulation revealed of a two-step mechanism of the nanoscale crystal formation. First, a partially layered silica embryo appeared, and then a more ordered crystalline layer with size larger than the critical nucleus size was formed. Subsequently, lithium ions piled up around the silicate layer and triggered stacking of adjacent silicate layers, which eventually built a perfect crystal. Contrarily to previous hypotheses, no lithium metasilicate crystal was observed as a precursor of the homogeneous crystallization of lithium disilicate.

DOI: [10.1103/PhysRevMaterials.5.075602](https://doi.org/10.1103/PhysRevMaterials.5.075602)

I. INTRODUCTION

Understanding the nucleation and crystallization processes in silicate melts and glasses is essential to design novel glass-ceramics materials with enhanced optical, mechanical, and chemical properties [1,2] and to prevent uncontrolled crystallization (devitrification) during glass production.

Several theories have been developed and refined to interpret the first key step, nucleation [3–8]. Classical nucleation theory (CNT), one of the most accepted, presumes that a critical crystal-like nucleus, with composition, structure, and properties of the final macroscopic phase, forms from random fluctuations of atomic arrangements in the melt. Therefore, in CNT the energy barrier for nucleation results from a change in size rather than composition and structure. This simplification limits the applicability to only simple crystallization, and it might be a reason why CNT severely underestimates the nucleation rates in silicate systems [3,9].

Alternative theories have been proposed to complement these limitations; in the generalized Gibbs approach (GGA) [10,11], it is assumed that the structure and properties of the nuclei can deviate from those of the macroscopic phases. This means that the nucleus structure can change during the growth, and, therefore, the final structure can be different from the original crystal structure. In GGA, the energy barrier for nucleation is not overcome by a change in size (as in CNT) but by a change in composition. Instead, in the two-step model [6], a temporal separation between the density and structural

fluctuations is assumed. First, local disordered regions with composition and density different from those of the initial liquid phase are formed, and then a structural reorganization inside this region leads to the appearance of the crystals.

In many cases, crystallization can evolve through a sequence of intermediate metastable configurations formed before the thermodynamically stable final crystalline phase appears [12–15].

Although these intermediate phases are often only transient, they play an important role in the crystallization pathway, and identifying their formation is crucial for controlling or inhibiting the formation of specific desired or undesirable phases, which would have a potential impact on the economic consequences as well for industry.

Among silicates, lithium disilicate (LS₂) has attracted huge fundamental and technological interest since it nucleates homogeneously with relatively high rates ($\approx 4.4 \times 10^9$ nuclei cm⁻³ s⁻¹ at 500 °C) and easily forms glass-ceramics products with enhanced chemical, mechanical, and thermal properties [16–19]. Several *in situ* characterization techniques have been applied to monitor the evolution of nucleation and crystallization processes to gain insight into fundamental aspects of crystallization in silicates [14,20–22]. However, contrary to the crystal growth, observing nucleation is extremely challenging since it occurs in the subnanometer length scales, which is often out of the experimental observable limit. Therefore, the crystallization pathway has not yet been understood from an atomistic viewpoint, and this major challenge remains active.

The major controversy concerning the crystallization kinetics in the LS₂ system is whether metastable phases appear

*Corresponding author: alfonso.pedone@unimore.it

or not prior to the formation of the thermodynamically stable crystal phase. Several experimental studies observed both the lithium metasilicate (LS) and the LS_2 crystals in the stoichiometric glass (see Fig. 1), whereas others observed only the latter one [14,20–22]. When observed, the LS crystal sustains only for a few hours at the nucleating temperature, and eventually disappears at higher temperature. A few studies postulated that the LS crystal nucleates first and subsequently promotes the heterogeneous LS_2 crystal on it [14,20], while the prior formation of metastable phases with stoichiometry close to the LS_2 composition (called α' - LS_2 and β' - LS_2) is also reported [23].

Molecular dynamics (MD) simulations overcome the length-scale problem faced in experiments and are thus powerful and indispensable tools to get insight into the nucleation process at the atomistic scale. Albeit, it is nowadays possible to study phenomena occurring in the microsecond timescale [24], it is still very challenging to follow nucleation in highly viscous melt because of the slow dynamics. Indeed, the time needed to observe spontaneous nucleation of LS_2 crystal in a simulation box of $1\text{--}2 \cdot 10^2 \text{ nm}^3$ would be $>10^{15} \text{ h}$, which is clearly impractical.

The seeding method, which artificially puts a nucleus in a melt, is a practical approach for low-viscous, not glass forming materials [5,25–30] and metallic glasses [31–33]. However, the method requires much longer time for silicate glasses because their crystallization would take hours even above the glass transition temperature. In a previous investigation we employed a seeding methodlike approach [34] to evaluate the nucleation free energy of the LS and LS_2 crystals in the LS_2 glass matrix but the crystallization pathway could not be observed in the simulations.

In this investigation, we overcome the time limitation of conventional MD simulations by applying the well-tempered metadynamics (WTMetaD) algorithm, which has been used in the past to drive nucleation and crystallization in low viscous liquids [35] and single elements [36–38]. Albeit, the silica melt to β -cristobalite transition was successfully investigated [39], the applicability to more complex layered binary silicates has not been demonstrated.

II. THEORETICAL BACKGROUND

In the WTMetaD [40,41], the free-energy landscape along a set of CVs, which are vector functions of the N particle positions, $s(r^N)$, is explored by periodically updating a history-dependent external potential $V(s)$ as

$$V_n(s) = V_{n-1}(s) + G(s, s_n) \exp\left[-\frac{1}{\gamma-1} \beta V_{n-1}(s_n)\right] \quad (1)$$

where γ is the bias factor, $\beta = 1/k_B T$ is the inverse temperature [the factor $(\gamma-1)\beta^{-1}$ is sometime referred to as $k_B \Delta T$] and $G(s, s_n)$ is a small repulsive biasing kernel (usually of Gaussian form) centered at the current CV values s_n . The biasing kernel is scaled by a factor, $\exp[-\frac{1}{\gamma-1} \beta V_{n-1}(s_n)]$, which decreases as $1/n$, and thus becomes smaller as the simulation progresses [40]. The iterative update of the bias potential is performed every N_G steps that correspond to a time interval $\tau_G = N_G dt$, where dt is the MD time step. It has been proven in [42] that long enough simulations can recover

the free-energy surface (FES) as

$$F(s) = -\left(\frac{\gamma}{\gamma-1}\right)V(s). \quad (2)$$

This approach allows recovering the FES along the biased collective variables s .

To recover the FES along different CVs not biased during the metadynamics simulations or to compute unbiased ensemble averages $\langle O(\mathbf{R}) \rangle$ (\mathbf{R} represents the atomic configurations of the system) a reweighting procedure has to be employed. The trajectory averages of the biased simulations are weighted according to the bias potential added during the metadynamics simulations in order to reconstruct the unbiased ensemble averages. In this work, the algorithm proposed by Tiwary *et al.* [43] is employed. The method evaluates the unbiased Boltzmann probability distribution $P_0(\mathbf{R})$ from the biased probability $P(\mathbf{R}, t)$ as

$$P_0(\mathbf{R}) = P(\mathbf{R}, t) e^{\beta[V(s(\mathbf{R}), t) - c(t)]}, \quad (3)$$

where the time-dependent function $c(t)$ is an estimator of the work done by the bias. It is computed by the formula [41]

$$c(t) = \frac{1}{\beta} \ln \frac{\int ds \exp\left[\frac{\gamma}{\gamma-1} \beta V(s, t)\right]}{\int ds \exp\left[\frac{1}{\gamma-1} \beta V(s, t)\right]}. \quad (4)$$

According to Eqs. (3) and (4), the average of a general observable $\langle O(\mathbf{R}) \rangle_0$ over the unbiased ensemble can be calculated from the metadynamics trajectory as

$$\langle O(\mathbf{R}) \rangle_0 = \langle O_b(\mathbf{R}) e^{\beta[V(s(\mathbf{R}), t) - c(t)]} \rangle, \quad (5)$$

where $O_b(\mathbf{R})$ is an observable in the biased ensemble and $e^{\beta[V(s(\mathbf{R}), t) - c(t)]}$ is the weight to rescale the biased simulations. Here the brackets $\langle \dots \rangle$ denote ensemble averages. As stated before, the reweighting method allows one to obtain the actual FES with a set of CVs by considering the function $O(\mathbf{R}) = \delta[s' - s'(\mathbf{R})]$, and the probability distribution at unbiased condition along the CVs is calculated as

$$\begin{aligned} P(s') &= \int d\mathbf{R} \delta[s' - s'(\mathbf{R})] P_0(\mathbf{R}) \\ &= \int d\mathbf{R} \delta[s' - s'(\mathbf{R})] P(\mathbf{R}, t) e^{\beta[V(s'(\mathbf{R}), t) - c(t)]} \end{aligned} \quad (6)$$

Then, the FES is then simply computed as

$$F(s') = -\frac{1}{\beta} \ln P(s'). \quad (7)$$

Note that the two FESs, one obtained by the reweighting procedure and the other one evaluated by Eq. (2), should be identical. Thereby the degree of coincidence between the two FESs can be an indicator to judge the convergence of the metadynamics simulations.

In highly viscous systems such as the silicate melt studied in this work, the proper sampling of the whole FES at low temperature is computationally very expensive since tens of microseconds of simulations would be required. In such a case, one possible alternative method is reweighting a high temperature distribution probability to a lower temperature one. To convert the temperature, the weights are dependent on the ensemble: $w(\mathbf{R}, V) = e^{(\beta-\beta')U(\mathbf{R})}$ and $w(\mathbf{R}, V) = e^{(\beta-\beta')U(\mathbf{R})+PV}$, for canonical (NVT) and isothermal-isobaric (NPT) ensembles, respectively, where β and β' are the old

and new inverse temperatures. Several primitive tests revealed that the potential energy is more effective than internal energy and enthalpy to obtain accurate FES by the temperature reweighting method since it is directly computed during the simulation. The reliability of temperature reweighting method is verified by studying the FES associated to the crystallization of β -cristobalite from silica melt, as shown in Sec. I of the Supplemental Material [44].

III. COMPUTATIONAL DETAILS

All simulations were performed using the large-scale atomic/molecular massively parallel simulator (LAMMPS) package [45] patched with the PLUMED 2 plugin [46]. The Nosé-Hoover thermostat [47] and barostat have been used to perform the MD simulations in an NPT ensemble. The relaxation time for the temperature was set to 0.1 ps, while the relaxation time for pressure was 10 ps with a target pressure of 1 bar. The pairwise PMMCS interatomic potentials developed by Pedone *et al.* [48] have been employed, using the Wolf summation method to treat long range Coulomb interactions [49]. The short-range interactions were evaluated with a cutoff distance of 5.5 Å. The equation of motion was integrated using the Verlet algorithm [50] with a time step of 2 fs.

The WTMetaD bias was constructed by accumulating Gaussians every 1 ps with width of 1 CV units and a height of 40 kJ/mol. The bias factor was set to 200. The length of the simulations was examined up to 23 μ s.

A. The simulation systems

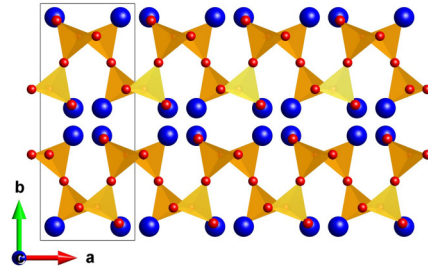
Figure 1 depicts the structural models used for the LS_2 crystal (named c- LS_2 hereafter), the LS_2 glass, and the lithium metasilicate (LS) crystals. The glass structures were obtained using the usual melt and quench approach [51] starting from the crystalline model of LS_2 , and the final simulation box was reshaped to match the experimental glass density. The systems were then heated and hold at 3500 K for 100 ps, which is enough to melt the samples and remove the memory of the initial configurations. The liquids were then monotonically cooled to 300 K with a cooling rate of approximately 5 K/ps. The cooled glass structures were subjected to a final equilibration run of 200 ps. In these cases, the NVT was employed, and a Berendsen thermostat [50] was used to control the temperature (frictional constants were set to 0.2 ps).

All the MetaD simulations were performed starting from a LS_2 melt containing 720 atoms whose initial structure was generated by replicating the c- LS_2 unit cell by $4 \times 1 \times 5$. To verify the size effect on the CVs used to drive the MetaD simulations, larger boxes obtained by replicating $5 \times 2 \times 5$ (1800 atoms) and $5 \times 3 \times 10$ (5400 atoms) were also examined [44].

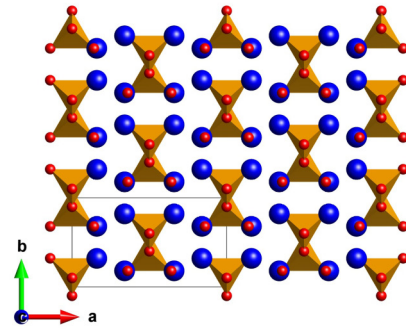
B. Choice of the CV to bias the simulations

The proper sampling of the rare events in the biased simulations strongly depends on the choice of the CVs, because they should effectively distinguish multiple stable and metastable states along the reaction pathway. In this work, the intensities of the x-ray diffraction (XRD) peaks were used as CVs to bias the system [39] because they represent important characteristics of the amorphous and crystal mi-

Lithium Disilicate (c- LS_2) - $Li_2Si_2O_5$



Lithium Metasilicate (LS) - Li_2SiO_3



Glass/Melt - $Li_2O \cdot 2SiO_2$

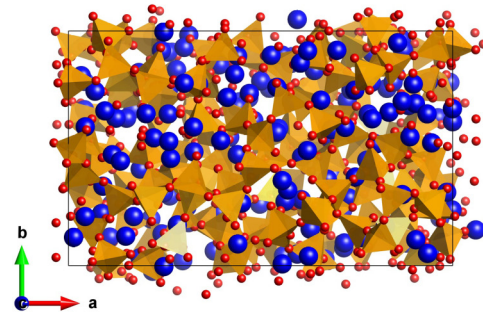


FIG. 1. Structure of the LS_2 glass, the c- LS_2 and LS crystals. Blue tetrahedral represents silicon, red and green spheres represent oxygen and lithium ions, respectively.

crostructures from short to middle ranges. The XRD intensity at the scattering vector \mathbf{Q} is computed using the Debye formula [52]

$$I(\mathbf{Q}) = \frac{1}{N} \sum_{j=1}^N \sum_{i=1}^N f_i(\mathbf{Q}) f_j(\mathbf{Q}) \frac{\sin(\mathbf{Q} \cdot \mathbf{r}_{ij})}{\mathbf{Q} \cdot \mathbf{r}_{ij}} W(\mathbf{r}_{ij}), \quad (8)$$

where N is the total number of atoms, $f_i(\mathbf{Q})$ and $f_j(\mathbf{Q})$ are the atomic scattering form factors, \mathbf{r}_{ij} is the distance vector between atoms i and j with a length of $r_{ij} = |\mathbf{r}_{ij}|$. $W(\mathbf{r}_{ij}) = \frac{\sin(\pi r_{ij}/R_c)}{\pi r_{ij}/R_c}$ is the Lorch function used to overcome the artifacts due to the finite simulation box, and R_c is the upper limit for r_{ij} . Contrary to the previous work by Niu *et al.* [39], which considered all the atoms to evaluate the XRD intensity, only silicon atoms were taken into account in this work to reduce the computational cost. This simplification does not sacrifice simulation accuracy because the less mobile silicon atoms

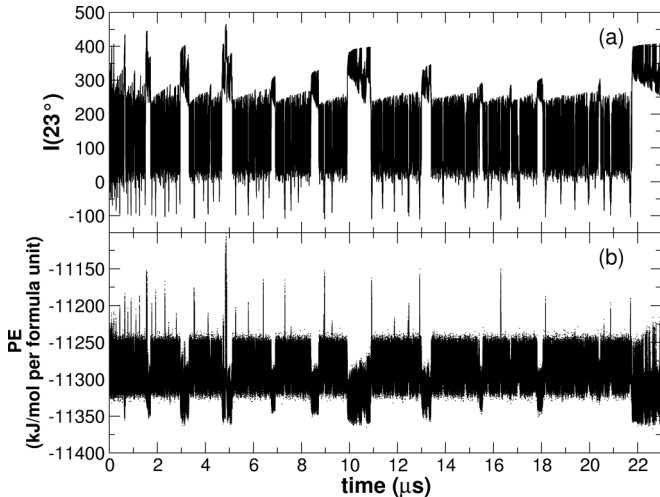


FIG. 2. Panel (a) reports the evolution of the intensity peak at $2\theta = 23^\circ$ and panel (b) reports the potential energy both along the $23 \mu\text{s}$ of WTMetaD simulations at 1800 K biased by $1CV$.

guided by the metadynamics scheme can bias the other atoms as well to promote crystallization. The intensities of the peaks at the scattering vectors ($Q = \frac{4\pi}{\lambda} \sin(2\theta/2)$) corresponding to $2\theta = 23^\circ$ and $2\theta = 35^\circ$ which are associated to the planes (040) and (002), respectively (see Sec. II and Figs. S1 and S2 of the Supplemental Material [44]) are selected as the most appropriate CVs [44]. These CVs allow us to discriminate the melt and the metasilicate LS and LS₂ crystals (see Fig. S2 [44]).

IV. RESULTS

A. Free energy surface

From the physical point of view, the melt-to-crystal transition process should be investigated at the melting temperature or below it since crystallization is thermodynamically favored for undercooled liquids.

The thermodynamic melting temperature of lithium disilicate determined using the coexisting phase method described in detail in the Supplemental Material [44] is estimated to be 1200 ± 50 K, which is in fair agreement with the experimental value of 1307 K [53]. However, as shown in [21], the mobility of silicon species in the time frames of tens of nanoseconds of MD simulations is extremely low at this temperature, hampering the efficient sampling of the free energy surface of the system.

To overcome this computational issue, we have performed the WTMetaD simulations at 1800 K for $23 \mu\text{s}$ and then performed a temperature rescaling to 1200 K, as described in detail in the theoretical section [44]. Figure S1 [44] clearly shows that this approach replicates FESs within the error of the converged MetaD simulations, confirming the applicability to lithium disilicate simulation.

Figure 2(a) shows the evolution of the biasing $I(23^\circ)$ collective variable at 1800 K, and Fig. S7 [44] reports the evolution of this CV at 1500, 1600, and 2000 K. As shown in Fig. 2(b), the potential energy decreases when $I(23^\circ)$ corresponds to the value of the c-LS₂ crystal, implying that

the jumps of the CVs effectively represent the melt-to-crystal transitions. This is also confirmed by visual inspection of the simulations and the analysis of the local order parameters that will be presented below. Several jumps between the amorphous and crystal phases were observed during the simulations at any temperature. The frequency of the transitions increases at higher temperature, but the persistence of crystalline structure shortens because at higher temperature the crystalline structure is less stable than the melt one. Contrarily, at lower temperature, the crystal phase persists for a longer period since the crystal structure becomes more stable. However, as anticipated above, the jump frequency reduces with temperature decreasing because of the reduced silicon diffusivity; therefore, longer simulations are required to accurately explore the FES at lower temperature.

The block analysis [54] performed on the WTMetaD at 1800 K reported in Fig. S8 and the comparison of the 1D FES computed by the reweighting method and by summing the biasing Gaussians (see Fig. S9) confirm that the simulation has reached convergence (the estimated error is 0.11 kJ/mol per formula unit). The 2D FES as functions of the biasing CV $[I(23^\circ)]$ and the unbiased second CV $[I(35^\circ)]$ at 1800 K is shown in Fig. 3(a).

Figure 3(b) shows the potential energy surface (PES) as a function of the two CVs computed by averaging along the trajectory at 1800 K, which is used to estimate the FES at 1200 K [see Fig. 3(c)] by temperature rescaling. The FES at 1800 K possesses a large absolute minimum at $I(23^\circ) \approx 150$ and $I(35^\circ) \approx 130$, which is associated to the melt state and the other shallower and less pronounced minimum at $I(23^\circ) \approx 320$ and $I(35^\circ) \approx 250$ corresponding to the c-LS₂ crystal. A flexion of the FES at (240; 150) is also observed.

The PES indicates that along the path from the melt to the crystal state intermediate states form, which will become more important at lower temperatures. Indeed, the melt state corresponds to a high potential energy region in the PES; the perfect c-LS₂ crystal phase corresponds to the absolute minimum whereas a second minimum at (300; 190) appears.

The FES at 1200 K shows that the minimum at the melt state does not change with temperature, whereas the FES near the crystalline state is substantially affected. The flexion of the curve at around (240; 150) unit becomes a shallow minimum whereas the crystalline minimum becomes deeper with decreasing the temperature, and the path from the melt state to the crystal becomes more structured, confirming that intermediate structure forms before the perfect crystalline structure appears.

The microstructures at the points A, B, C, and D highlighted in Fig. 3 are shown in Fig. 4 and reveal that the intermediate structures are layered disordered structures. Indeed, a few silicon atoms are displaced from the positions in the c-LS₂ crystal. For instance, some Si ions connect the double layers or disrupt the apparent short 4 T chain of the layers, as shown by the green tetrahedral units in Figs. 4(b) and 4(c). Iqbal *et al.* [21] observed the formation of two LS₂ phases (α' and β') before the stable crystal. They have attributed α' -LS₂ to a structure ($P2_1$ space group) with a unit cell half of the c-LS₂ crystal, while the β' phase was more disordered.

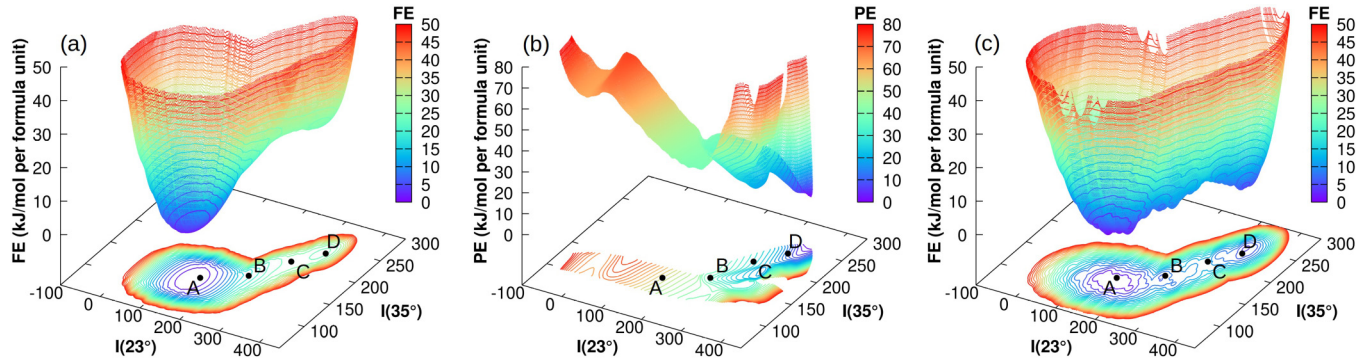


FIG. 3. (a) Reweighted 2D FES along biased $I(23^\circ)$ and unbiased $I(35^\circ)$ at 1800 K, (b) potential energy surface obtained from the simulation at 1800 K, and (c) 2D FES at 1200 K computed with a rescaling of the temperature from the simulation at 1800 K.

B. Analysis of the crystallization mechanism at atomic level

To distinguish the silicon environments in the LS_2 glass, LS_2 , and the LS crystals we have computed the individual six-order Steinhardt order parameters (Q_6) [8], the average $\bar{Q}_6(i)$, and local average $\bar{Q}_6^{loc}(i)$ parameter for silicon atom i .

The individual l -order Steinhardt parameter for atom i is defined by

$$Q_l(i) = \sqrt{\frac{4\pi}{2l+1} \sum_{m=-l}^l |q_{lm}(i)|^2} \quad (9)$$

with

$$q_{lm}(i) = \frac{1}{N(i)} \sum_{j=1}^{N(i)} Y_{lm}(r_{ij}), \quad (10)$$

where the index j runs on the $N(i)$ neighbors of atom i within a certain cutoff (R_1). $Y_{lm}(r_{ij})$ is a spherical harmonic with a vector displacement r_{ij} from atoms i and j . The subscript l is a

free integer parameter that confines m between $-l$ and $+l$. The average $\bar{Q}_6(i)$ is the average of the individual Q_6 parameters for the neighbors of atom i within a certain cutoff (R_2).

The local $\bar{Q}_6^{loc}(i)$ parameter is computed by taking the dot product between the q_6 vector on the central atom and the q_6 vector on the atoms in the first coordination sphere:

$$\bar{Q}_6^{loc}(i) = \frac{1}{N(i)} \sum_{j=1}^{N(i)} \sum_{m=-6}^6 q_{6m}(i)q_{6m}(j). \quad (11)$$

This parameter measures the extent to which the orientation of the atoms j in the first coordination sphere of atom i match the orientation of the central atom.

The average $\bar{Q}_6(i)$ and local average $\bar{Q}_6^{loc}(i)$ parameter for atom i is the average of the Q_6 and \bar{Q}_6^{loc} parameters of its neighboring atoms within a certain radius (R_2). The probability distributions of these parameters for Si ions in the LS_2 glass, c- LS_2 , and LS crystals at 1600 K are reported in Fig. 5. The figure shows that using as cutoffs $R_1 = 6 \text{ \AA}$ and $R_2 = 3.75 \text{ \AA}$ the individual Q_6 parameter is not able to distinguish the glass to the LS_2 crystals whereas the other parameters can distinguish the glass to the LS_2 and LS crystals.

In particular, silicon ions exhibit well-separated \bar{Q}_6^{loc} distributions approximately ranging $(-0.4-0.2)$, $(0.2-0.7)$, and $(0.7-0.9)$ for the melt, c- LS_2 , and LS crystals, respectively, without significant overlap. That means that the local structure around each silicon ion can be assigned to one of them. The \bar{Q}_6^{loc} values for the silicon ions were divided into three categories ranging $-0.4-0.2$, $0.2-0.68$, and $0.69-1.0$, to measure the fraction of silicon ions with local structure similar to melt, c- LS_2 , and LS crystal, respectively.

After having defined the proper local order parameters to follow the crystallization pathway and mechanism at the atomic level we conducted 12 μs WTMetaD simulations at 1500 and 1600 K. At this temperature melt-to-crystals transitions are less frequent compared to the case at 1800 K due to the slower diffusion of the atoms but this allowed us to better follow the sequential steps leading to the crystal formation. All the transitions reported in Fig. S10 [44] were considered, but a representative transition is highlighted in Fig. 6.

Figure 6(a) reports the evolution of the intensity of the two peaks at $2\theta = 23^\circ$ and 35° ; 6(b) is the fraction of silicon ions connected to n neighboring silicon ions through bridging oxygen (Si^n : n is the number of Si-O-Si links of the central Si

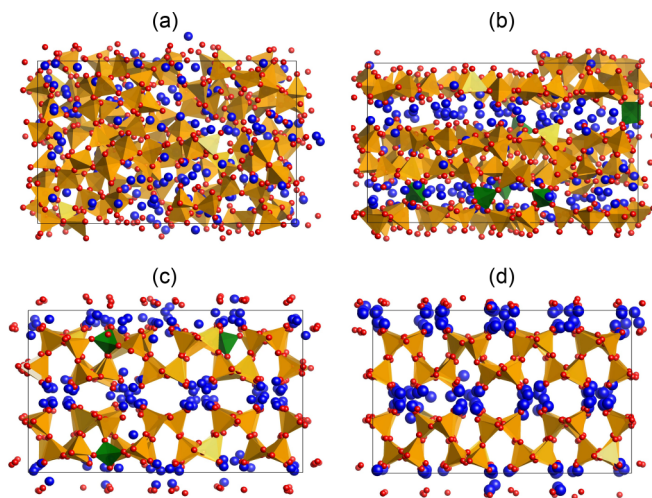


FIG. 4. Snapshots representative of the structure of the system at $[I(23^\circ); I(35^\circ)]$ (130;132) (a), (240;160) (b), (300;200) (c) and (320;220) (d) units extracted from WTMetaD simulations at 1600 K. Blue atoms represent lithium, red ones are oxygen, and yellow and green tetrahedral are silicon.

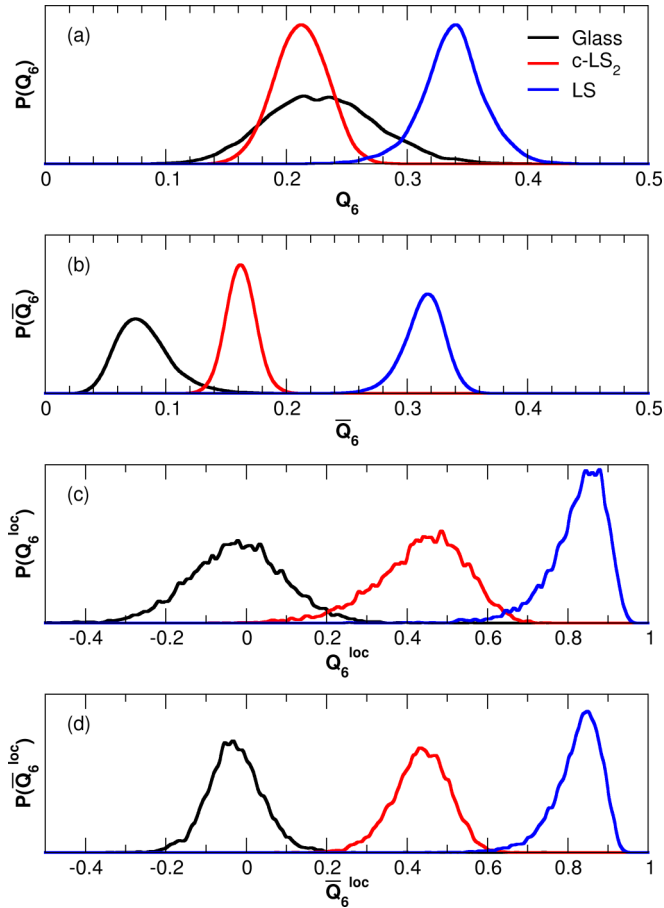


FIG. 5. Probability distributions of the Q_6 , local Q_6^{loc} , average \bar{Q}_6 and local average \bar{Q}_6^{loc} parameters of silicon ions in the LS_2 glass, c- LS_2 , and LS crystals at 1600 K. These parameters have been computed considering only silicon ions in the coordination sphere of the central Si ion using $R_1 = 6 \text{ \AA}$ and $R_2 = 3.75 \text{ \AA}$.

ion); 6(d) is the population of silicon ions with local structure similar to melt, c- LS_2 , and LS crystal (defined using the average \bar{Q}_6^{loc} Steinhardt parameter) between 0.55 and 0.75 μs of the simulation at 1600 K in which a melt-to-crystal transition occurs.

According to the local averaged \bar{Q}_6^{loc} parameter [Fig. 6(d)], almost all the silicon is in the melted condition up to 0.62 μs . At around 0.62 μs , $I(23^\circ)$ suddenly increases to about 250–300 units. Simultaneously, the percentage of Si^3 species as well as the \bar{Q}_6^{loc} value averaged over all silicon ions start to increase. In addition, the ratio of silicon ions with environment similar to the LS_2 crystals increases to 10%, implying that a critical crystal nucleus appears in the melt and starts to grow. Interestingly, $I(35^\circ)$ is still fluctuating at around the value close to that assumed in the melt up to 0.65 μs , indicating that the crystal nucleus is still disordered and it needs to cross another energy barrier to become ordered. In other words, metadynamics simulations explore a variety of intermediate states during the melt-to-crystal transition. Several representative snapshots of the structures of (A) the melt state, (B) an initial nucleus, (C) a layered but disordered structure, and (D) an almost perfect c- LS_2 crystal are displayed in the right panels of Fig. 6. In these snapshots, only silicon ions are

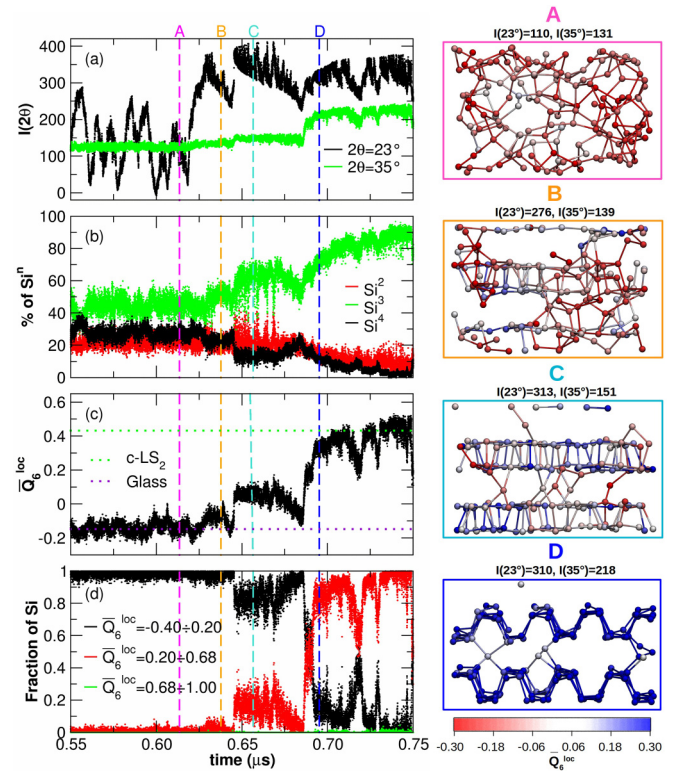


FIG. 6. Evolution of (a) $I(23^\circ)$ and $I(35^\circ)$, (b) distribution of Si^n species, (c) \bar{Q}_6^{loc} averaged over all Si atoms and (d) distribution of the Si ions with LS_2 glass, LS_2 , and LS crystal-like environments determined using the local average \bar{Q}_6^{loc} Steinhardt parameter during WTMetaD simulations at 1600 K. The analysis has been performed between 0.55 and 0.75 μs of the trajectory for clarity. On the right are reported the structures extracted from the simulation corresponding to the points indicated with the dashed line in the left graphs. Only Si atoms are shown and are colored according to their value of \bar{Q}_6^{loc} .

displayed in color representing the \bar{Q}_6^{loc} value. A movie of the crystallization event is reported in the Supplemental Material (see MovieS1.mov file) [44].

To measure the crystal-like cluster size along the WTMetaD simulations, we computed the adjacency matrix among Si ions with LS_2 crystal-like \bar{Q}_6^{loc} values and used a depth first search algorithm [55] to find the number of Si ions (N_{Si}) in the clusters. The sizes of the two largest clusters were evaluated, as shown in Fig. 7. The number of Si ions in the two largest clusters fluctuates around 15–20 at maximum in the melt state, indicating formation and dissolution of crystal-like tiny embryos. When the crystallization starts, two critical nuclei with about 15–30 and 8–15 silicon appear, as shown in Fig. 7. MovieS2 of the Supplemental Material [44] shows a nucleation event at the atomic level. Especially, the largest cluster seems to dispose the tetrahedral SiO_4 units in partial layered structure topologically similar to that of the LS_2 crystals. The size gradually increases until about 0.65 μs , where $I(35^\circ)$ apparently increases, as shown in Fig. 6.

The second largest nucleus appears simultaneously and locates near the largest one. Then, the two adjacent nuclei coalesce each other to form a larger crystal-like structure possessing an almost complete 2 T layer composed of about 40

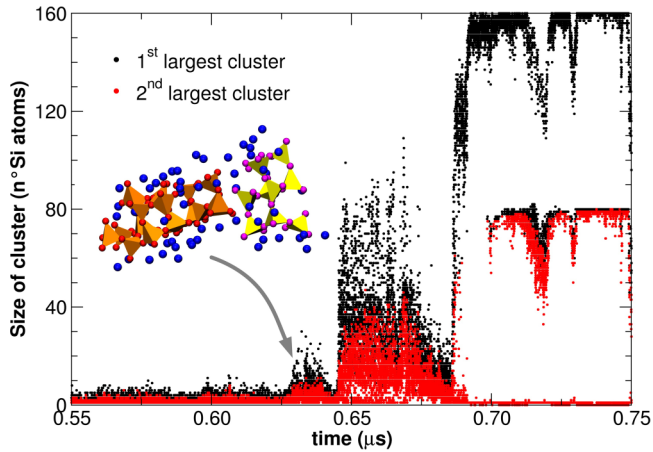


FIG. 7. Evolution of the size of the two biggest LS_2 crystal-like clusters of Si ions along a crystallization event during WTMetaD simulations at 1600 K. The insets show the structure of the first (orange tetrahedral: 18 Si atoms) and second (yellow tetrahedral: 10 Si atoms) larger clusters found.

silicon ions. At the same time, lithium ions around the nucleus (blue spheres in Fig. 7) formed layered structures and promote the formation of the second silica layer. Consequently, the initial nucleus grows further in a stepwise fashion. After that, both two largest nuclei are enlarged with approximately 80 silicon ions, indicating that the two silicate layers are completely formed. Following the formation of two layers, the largest cluster size goes back and forth between 80 and 160, implying that some disordered silicon ions connect the two layers, as already shown in Fig. 4(b).

According to the cluster analysis along all the simulations, the critical nucleus size contains between 20 and 40 silicon ions. This agrees well with our previous investigation exploiting a modified seeding method [34], which estimated the critical nucleus with 26 silicon ions. It worthwhile to highlight that metadynamics simulations do not allow us to determine the real transient time of the disordered layered structure which promotes the formation of the perfect crystal but reveals that the initial nucleus has a layered disordered structure instead of the spherical perfect crystalline one assumed in CNT.

In summary, state-of-the art metadynamics simulations show that crystallization in the LS_2 system does not rigorously follow CNT assumptions and occurs following several cooperative steps, which lowers the energy barrier for nucleation.

The other interesting finding is that any LS germ was observed prior to the c- LS_2 crystallization implying that a

LS nucleus is not a necessary precursor of the c- LS_2 precipitation (at least for stoichiometric LS_2 melts), contrary to previous suggestions [20,22,23]. This is also consistent with our previous MD investigation, which found that the chainlike microstructures with stoichiometry of LS crystal are formed only at the glass surface [34].

V. CONCLUSIONS

In conclusion, we showed that metadynamics is a powerful technique to study nucleation and crystallization in multi-component oxide glasses and glass ceramics, even when the crystal possesses an anisotropic layered structure. The biased simulations successfully visualize the process of the crystal formation in detail, and the FES can be obtained in a wide range of dimensional space. This study also demonstrates that the temperature-rescaling method is useful to obtain FES at temperature lower than the melting temperature of the glass, which can overcome the limitation of simulation time required at such a highly viscous condition. Therefore, the procedure verified is expected to be also useful for shedding light on the genesis of magmatic rocks and to study geochemical processes.

Contrarily, the cutting-edge method, WTMetaD, still exhibits several limitations for studying nucleation and crystallization in highly viscous glass forming systems: (i) the model size is still limited up to thousands of atoms, and the adverse effect of periodic boundary conditions on the crystallization process is expected; (ii) the employment of temperatures higher than the melting point might prevent the observation of alternative crystallization pathways at lower temperature. Longer simulations and a more efficient algorithm are necessary to overcome both the limitations. Future efforts will be dedicated to these issues.

The data that support the findings of this work are available from the corresponding author upon reasonable request.

ACKNOWLEDGMENTS

We acknowledge Prof. H. Niu for fruitful discussions. AGC Inc. supported the work.

F.L. and F.T. performed the simulations, analysis, and movies. M.C.M., K.M., Y.T., and S.U. read and revised the manuscript. A.P. devised the work and wrote the manuscript.

The authors declare no competing financial or nonfinancial interests.

[1] J. C. Mauro, C. S. Philip, D. J. Vaughn, and M. S. Pambianchi, Glass science in the united states: Current status and future directions, *Int. J. Appl. Glass Sci.* **5**, 2 (2014).
 [2] L. Li, H. Lin, S. Qiao, Y. Zou, S. Danto, K. Richardson, J. D. Musgraves, N. Lu, and J. Hu, Integrated flexible chalcogenide glass photonic devices, *Nat. Photonics* **8**, 643 (2014).

[3] L. Cormier, Nucleation in glasses – new experimental findings and recent theories, *Proc. Mater. Sci.* **7**, 60 (2014).
 [4] K. F. Kelton, Crystal nucleation in liquids and glasses, in *Solid State Physics*, edited by H. Ehrenreich and D. Turnbull (Academic, New York, 1991), Vol. 45, pp. 75–177.
 [5] G. C. Sosso, J. Chen, S. J. Cox, M. Fitzner, P. Pedevilla, A. Zen, and A. Michaelides, Crystal nucleation in liquids: Open

- questions and future challenges in molecular dynamics simulations, *Chem. Rev.* **116**, 7078 (2016).
- [6] P. G. Vekilov, Nucleation, *Cryst. Growth Des.* **10**, 5007 (2010).
- [7] V. M. Fokin, A. S. Abyzov, E. D. Zanotto, D. R. Cassar, A. M. Rodrigues, and J. W. P. Schmelzer, Crystal nucleation in glass-forming liquids: Variation of the size of the “structural units” with temperature, *J. Non-Cryst. Solids* **447**, 35 (2016).
- [8] J. Deubener, Structural aspects of volume nucleation in silicate glasses, *J. Non-Cryst. Solids* **351**, 1500 (2005).
- [9] S. Sen and T. Mukerji, A generalized classical nucleation theory for rough interfaces: Application in the analysis of homogeneous nucleation in silicate liquids, *J. Non-Cryst. Solids* **246**, 229 (1999).
- [10] J. W. P. Schmelzer, G. Sh. Boltachev, and V. G. Baidakov, Classical and generalized Gibbs’ approaches and the work of critical cluster formation in nucleation theory, *J. Chem. Phys.* **124**, 194503 (2006).
- [11] J. W. P. Schmelzer, A. R. Gokhman, and V. M. Fokin, Dynamics of first-order phase transitions in multicomponent systems: A new theoretical approach, *J. Colloid Interface Sci.* **272**, 109 (2004).
- [12] C. Guo, J. Wang, J. Li, Z. Wang, and S. Tang, Kinetic pathways and mechanisms of two-step nucleation in crystallization, *J. Phys. Chem. Lett.* **7**, 5008 (2016).
- [13] D. Gebauer, M. Kellermeier, J. D. Gale, L. Bergström, and H. Cölfen, Pre-nucleation clusters as solute precursors in crystallization, *Chem. Soc. Rev.* **43**, 2348 (2014).
- [14] L. L. Burgner, M. C. Weinberg, P. Lucas, P. C. Soares, and E. D. Zanotto, XRD investigation of metastable phase formation in $\text{Li}_2\text{O}-2\text{SiO}_2$ Glass, *J. Non-Cryst. Solids* **255**, 264 (1999).
- [15] C. Bischoff, H. Eckert, E. Apel, V. M. Rheinberger, and W. Höland, Phase evolution in lithium disilicate glass-ceramics based on non-stoichiometric compositions of a multi-component system: Structural studies by ^{29}Si single and double resonance solid state NMR, *Phys. Chem. Chem. Phys.* **13**, 4540 (2011).
- [16] W. Höland, E. Apel, C. h. van’t Hoen, and V. Rheinberger, Studies of crystal phase formations in high-strength lithium disilicate glass-ceramics, *J. Non-Cryst. Solids* **352**, 4041 (2006).
- [17] Z. Khalkhali, B. E. Yekta, and V. K. Marghussian, Mechanical and chemical properties of Zr and P-Doped lithium disilicate glass ceramics in dental restorations, *Int. J. Appl. Ceram. Technol.* **9**, 497 (2012).
- [18] T. Zhao, Y. Qin, P. Zhang, B. Wang, and J.-F. Yang, High-performance, reaction sintered lithium disilicate glass-ceramics, *Ceram. Int.* **40**, 12449 (2014).
- [19] S. D. Stookey, Catalyzed crystallization of glass in theory and practice, *Ind. Eng. Chem.* **51**, 805 (1959).
- [20] L. L. Burgner, P. Lucas, M. C. Weinberg, P. C. Soares, and E. D. Zanotto, On the persistence of metastable crystal phases in lithium disilicate glass, *J. Non-Cryst. Solids* **274**, 188 (2000).
- [21] P. C. Soares, E. D. Zanotto, V. M. Fokin, and H. Jain, TEM and XRD study of early crystallization of lithium disilicate glasses, *J. Non-Cryst. Solids* **331**, 217 (2003).
- [22] R. S. Soares, R. C. C. Monteiro, M. M. R. A. Lima, and R. J. C. Silva, Crystallization of lithium disilicate-based multicomponent glasses – effect of silica/lithia ratio, *Ceram. Int.* **41**, 317 (2015).
- [23] Y. Iqbal, W. E. Lee, D. Holland, and P. F. James, Crystal nucleation in P_2O_5 -doped lithium disilicate glasses, *J. Mater. Sci.* **34**, 4399 (1999).
- [24] K. Lindorff-Larsen, S. Piana, R. O. Dror, and D. E. Shaw, How fast-folding proteins fold, *Science* **334**, 517 (2011).
- [25] G. C. Sosso, T. F. Whale, M. A. Holden, P. Pedevilla, B. J. Murray, and A. Michaelides, Unravelling the origins of ice nucleation on organic crystals, *Chem. Sci.* **9**, 8077 (2018).
- [26] J. R. Espinosa, C. Vega, C. Valeriani, and E. Sanz, Seeding Approach to Crystal Nucleation, *J. Chem. Phys.* **144**, 034501 (2016).
- [27] L. Separdar, J. P. Rino, and E. D. Zanotto, Molecular dynamics simulations of spontaneous and seeded nucleation and theoretical calculations for zinc selenide, *Comput. Mater. Sci.* **187**, 110124 (2021).
- [28] A. O. Tipseev, E. D. Zanotto, and J. P. Rino, Crystal nucleation kinetics in supercooled germanium: MD simulations versus experimental data, *J. Phys. Chem. B* **124**, 7979 (2020).
- [29] B. Yu, Y. Liang, Z. Tian, R. Liu, T. Gao, Q. Xie, and Y. Mo, MD simulation on crystallization mechanisms of rapidly supercooled Fe-Ni alloys, *J. Cryst. Growth* **535**, 125533 (2020).
- [30] S. C. C. Prado, J. P. Rino, and E. D. Zanotto, Successful test of the classical nucleation theory by molecular dynamic simulations of BaS, *Comput. Mater. Sci.* **161**, 99 (2019).
- [31] P. K. Bommineni, M. Klement, and M. Engel, Spontaneous Crystallization in Systems of Binary Hard Sphere Colloids, *Phys. Rev. Lett.* **124**, 218003 (2020).
- [32] C. Desgranges and J. Delhommelle, Unusual Crystallization Behavior Close to the Glass Transition, *Phys. Rev. Lett.* **120**, 115701 (2018).
- [33] Y. Sun, H. Song, F. Zhang, L. Yang, Z. Ye, M. I. Mendelev, C.-Z. Wang, and K.-M. Ho, Overcoming the Time Limitation in Molecular Dynamics Simulation of Crystal Nucleation: A Persistent-Embryo Approach, *Phys. Rev. Lett.* **120**, 085703 (2018).
- [34] F. Lodesani, M. C. Menziani, K. Maeda, Y. Takato, S. Urata, and A. Pedone, Disclosing crystal nucleation mechanism in lithium disilicate glass through molecular dynamics simulations and free-energy calculations, *Sci. Rep.* **10**, 17867 (2020).
- [35] D. Quigley and P. M. Rodger, A metadynamics-based approach to sampling crystallisation events, *Mol. Simul.* **35**, 613 (2009).
- [36] Y.-Y. Zhang, H. Niu, G. Piccini, D. Mendels, and M. Parrinello, Improving collective variables: The case of crystallization, *J. Chem. Phys.* **150**, 094509 (2019).
- [37] H. Niu, L. Bonati, P. M. Piaggi, and M. Parrinello, Ab initio phase diagram and nucleation of gallium, *Nat. Commun.* **11**, 2654 (2020).
- [38] L. Bonati and M. Parrinello, Silicon Liquid Structure and Crystal Nucleation from Ab Initio Deep Metadynamics, *Phys. Rev. Lett.* **121**, 265701 (2018).
- [39] H. Niu, P. M. Piaggi, M. Invernizzi, and M. Parrinello, Molecular dynamics simulations of liquid silica crystallization, *Proc. Natl. Acad. Sci. U.S.A.* **115**, 5348 (2018).
- [40] A. Barducci, G. Bussi, and M. Parrinello, Well-Tempered Metadynamics: A Smoothly Converging and Tunable Free-Energy Method, *Phys. Rev. Lett.* **100**, 020603 (2008).
- [41] O. Valsson, P. Tiwary, and M. Parrinello, Enhancing important fluctuations: Rare events and metadynamics from a conceptual viewpoint, *Annu. Rev. Phys. Chem.* **67**, 159 (2016).

- [42] J. F. Dama, M. Parrinello, and G. A. Voth, Well-Tempered Metadynamics Converges Asymptotically, *Phys. Rev. Lett.* **112**, 240602 (2014).
- [43] P. Tiwary and M. Parrinello, A time-independent free energy estimator for metadynamics, *J. Phys. Chem. B* **119**, 736 (2015).
- [44] See Supplemental Material at <http://link.aps.org/supplemental/10.1103/PhysRevMaterials.5.075602> for a detailed description of the computational details used to perform the simulations and analysis; investigation of the effects of the subset of atoms used to compute the XRD patterns and its dependency to the size and temperature; evolution of the intensity of the peak at $2\theta = 23^\circ$ and the potential energy; movies of the nucleation and crystallization of the lithium disilicate crystal from melt. This Supplemental Material includes Refs. [27,34,39,48,54,56,57].
- [45] S. Plimpton, Fast parallel algorithms for short-range molecular dynamics, *J. Comput. Phys.* **117**, 1 (1995).
- [46] G. A. Tribello, M. Bonomi, D. Branduardi, C. Camilloni, and G. Bussi, PLUMED 2: New feathers for an old bird, *Comput. Phys. Commun.* **185**, 604 (2014).
- [47] D. J. Evans and B. L. Holian, The nose–hoover thermostat, *J. Chem. Phys.* **83**, 4069 (1985).
- [48] A. Pedone, G. Malavasi, M. C. Menziani, A. N. Cormack, and U. Segre, A new self-consistent empirical interatomic potential model for oxides, silicates, and silica-based glasses, *J. Phys. Chem. B* **110**, 11780 (2006).
- [49] D. Wolf, P. Keblinski, S. R. Phillpot, and J. Eggebrecht, Exact method for the simulation of coulombic systems by spherically truncated, pairwise R⁻¹ summation, *J. Chem. Phys.* **110**, 8254 (1999).
- [50] M. P. Allen, M. P. Allen, D. J. Tildesley, and D. J. Tildesley, *Computer Simulation of Liquids* (Clarendon, Oxford, 1989).
- [51] A. Pedone, Properties calculations of silica-based glasses by atomistic simulations techniques: A review, *J. Phys. Chem. C* **113**, 20773 (2009).
- [52] P. Debye, Zerstreung von röntgenstrahlen, *Ann. Phys.* **351**, 809 (1915).
- [53] E. D. Zanotto, J. E. Tsuchida, J. F. Schneider, and H. Eckert, Thirty-Year quest for structure–nucleation relationships in oxide glasses, *Int. Mater. Rev.* **60**, 376 (2015).
- [54] G. Bussi, and G. A. Tribello, Analyzing and Biasing Simulations with PLUMED, in *Biomolecular Simulations: Methods and Protocols*, edited by M. Bonomi and C. Camilloni, (Springer, New York, 2019), pp. 529–578.
- [55] G. A. Tribello, F. Giberti, G. C. Sosso, M. Salvalaglio, and M. Parrinello, Analyzing and driving cluster formation in atomistic simulations, *J. Chem. Theory Comput.* **13**, 1317 (2017).
- [56] E. T. Chen, R. N. Barnett, and U. Landman, Crystal-Melt and melt-vapor interfaces of nickel, *Phys. Rev. B* **40**, 924 (1989).
- [57] W. Zhang, Y. Peng, and Z. Liu, Molecular dynamics simulations of the melting curve of NiAl Alloy under pressure, *AIP Adv.* **4**, 057110 (2014).